Supporting Information for

In situ growth of Fe and Nb co-doped Ni(OH)₂ nanosheet arrays on nickel foam for the efficient oxygen evolution reaction

Junjie Pan [a], Shaoyun Hao [a], Xingwang Zhang [a*], Rongxin Huang [b*]

[*]Corresponding author.

[a] *Key Laboratory of Biomass Chemical Engineering of Ministry of Education, College of Chemical and Biological Engineering Zhejiang University, Hangzhou 310027, Zhejiang Province, China.* E-mail: xwzhang@zju.edu.cn

[b] *South China Institute of Environmental Science, Ministry of Environmental Protection, Guangzhou 510655, Guangdong Province, China.* E-mail: huangrongxinhit@163.com

Contents

Experimental Details

NaCl, FeCl$_3$·6H$_2$O, ethanol, and acetone were got from Sinopharm Chemical Reagent Co., Ltd. NbCl$_5$ and commercial IrO$_2$/C (20%) were taken from Shanghai Maclin Biochemical Co., Ltd.

All of the electrochemistry measurements were performed by standard three-electrode system. Graphite rod and Hg/HgO electrode were served as the counter electrode, and the reference electrode, respectively. The self-fabricated electrode was cut into 1×1 cm^2 as the working electrode. The measured potentials were converted to the potentials versus reversible hydrogen electrode (vs. RHE) based on the following Eq. (1). E$_{RHE}$ is the potential versus RHE, E$_{Hg/HgO}$ is the measured potentials against the reference electrode, and E$^o_{Hg/HgO}$ is 0.098 V at 25 °C.

$$E_{RHE} = E_{Hg/HgO} + 0.059pH + E^o_{Hg/HgO} \qquad (1)$$

Before all of the electrochemistry measurements, the reference electrode was RHE corrected by using Pt wire as work electrode and graphite rod as counter electrode. CV test was carried out on the system for 5 circles. Take the average value of potentials at current density of 0 mA cm^{-2}. Comparing the average value with standard potential value to correct reference electrode potential.

Polarization curves were measured at a scan rate of 5 mV s^{-1} with iR compensation. The Tafel slopes were obtained from the corresponding polarization curves based on the following Eq. (2). Here η is potential vs. RHE, j is current density and b is Tefel slope.

$$\eta = b \cdot \log j + a \qquad (2)$$

Electrochemical impedance spectroscopy (EIS) were measured at frequencies ranging from 10 mHz to100 kHz. Charge transfer resistance (R$_{ct}$) of the electrode was analyzed by ZSimpWin software.

The stability of the electrode was evaluated by chronopotentiometric measurement at 50 mA cm^{-2}

Calculation of ECSA

The electrochemically active surface area (ECSA) was evaluated by double-layer the capacitance (C$_{dl}$). The C$_{dl}$ of the catalysts were obtained by cyclic voltammetry (CV) at non-faradic region with various scan rates. The C$_{dl}$ was estimated $\Delta j = (j_a - j_c)$

against the scan rate, and the slope is twice of the C_{dl}.

ECSA is calculated by dividing C_{dl} by specific capacitance value. The capacitance value is always taken to be about 20-60 μm cm^{-2}. Here, 40 μm cm^{-2} is selected for the calculation of ECSA.

Calculation of Faradic efficiency

To measuring Faradic efficiency of the catalyst, galvanostatic catalysis was performed at a current density of 10 mA cm^{-2} after injecting N_2 into the seal reactor for 30 minutes. The produced O_2 was quantitatively detected by FULI GC9790II gas chromatograph every 20 minutes. The spectra were obtained by a thermal conductivity detector (TCD) at injection temperature of 80 °C.

Calculation of specific activity normalized by ECSA

The specific activity normalized by ECSA is calculated by the following Eq (3). Here, j_{ECSA} is the specific activity normalized by ECSA, j is current density, ECSA is the electrochemically active surface area calculated above.

$$j_{ECSA} = j \ / \ (ECSA) \tag{3}$$

Calculation of TOFs

Turnover frequency (TOF) was calculated based on the following Eq. (4). Here j is the current density, A is the geometric surface area of the electrode,4 stands for the four electron transfer for each O_2 molecule, F is the Faraday constant 96485 C mol^{-1}, n is the moles of metal atoms on the electrode.

$$TOF = j \times A \ / \ (4 \times F \times n) \tag{4}$$

Computaional Details

The computational hydrogen electrode (CHE) model[1] was used to calculate the Gibbs reaction free energy change (ΔG) for each step in the four-electron oxygen evolution reaction. According to the CHE model, the ΔG value was gained by the following Eq (5).

$$\triangle G = \Delta E_{DFT} + \Delta E_{zpe} - T\Delta S + eU + \Delta G_{pH} \tag{5}$$

where ΔE_{DFT} is the reaction energy, ΔE_{ZPE} and ΔS are the changes in zero point energy and entropy at 298.15k, respectively. T, e and U are the temperature, the

number of electrons transferred and the electrode potential, respectively. The ΔG_{pH} is the free energy correction of pH, which can be calculate by the following Eq (6).

$$\Delta G_{pH}=k_B \, T \times \ln 10 \times pH \tag{6}$$

where the k_B is the Boltzman constant, and the pH was set to be zero in this calculation.

The rate-determining step (RDS) is determined by the step which possessed the largest Gibbs reaction free energy change (ΔG_{max}).
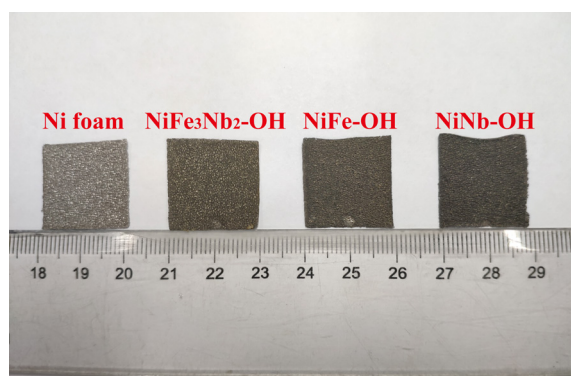
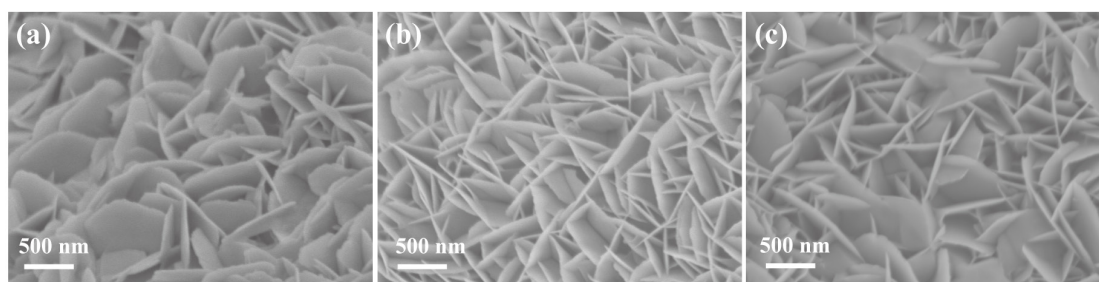**Fig. S1.** Digital photo of as prepared blank Ni foam, NiFe$_3$Nb$_2$-OH, NiFe-OH and NiNb-OH.

Fig. S2. SEM images of (a) NiFe$_1$Nb$_4$-OH, (b) NiFe$_2$Nb$_3$-OH and (c) NiFe$_4$Nb$_1$-OH.
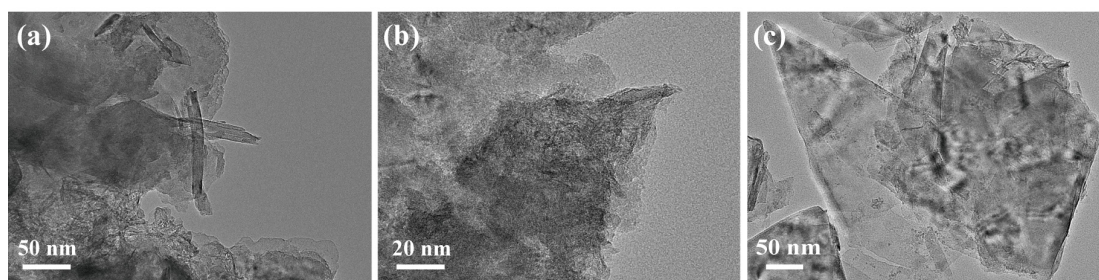
Fig. S3. TEM images of (a) NiFe$_1$Nb$_4$-OH, (b) NiFe$_2$Nb$_3$-OH and (c) NiFe$_4$Nb$_1$-OH
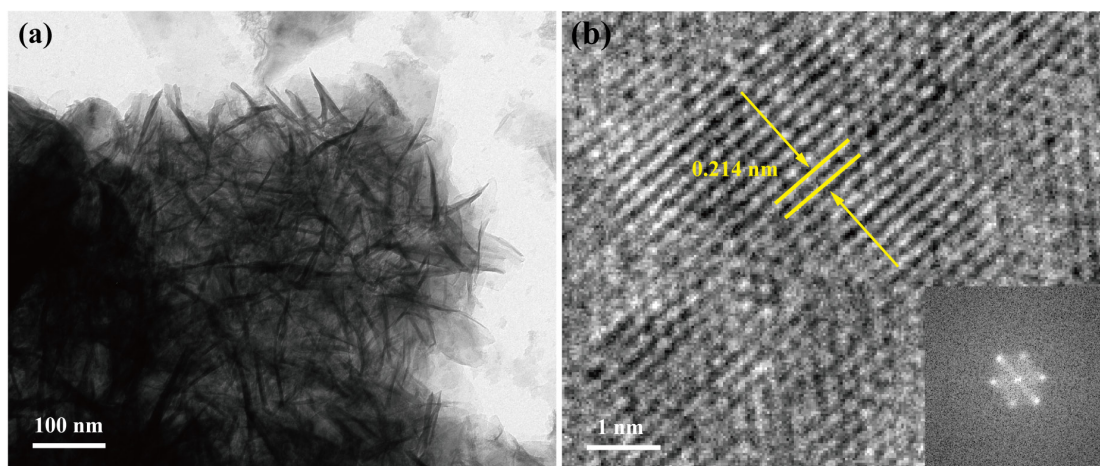
Fig. S4. (a) TEM image and (b) HRTEM image of NiFe-OH (inset: the corresponding FFT transfer).
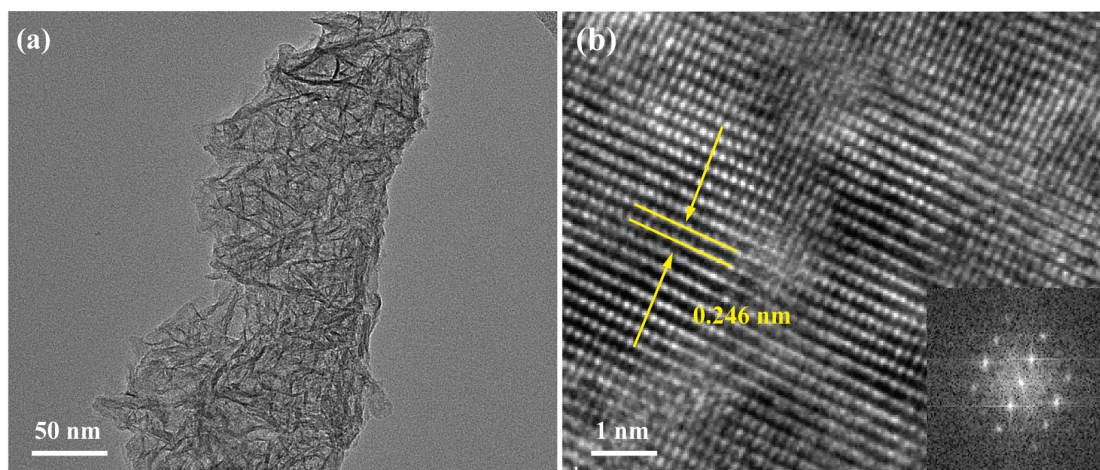

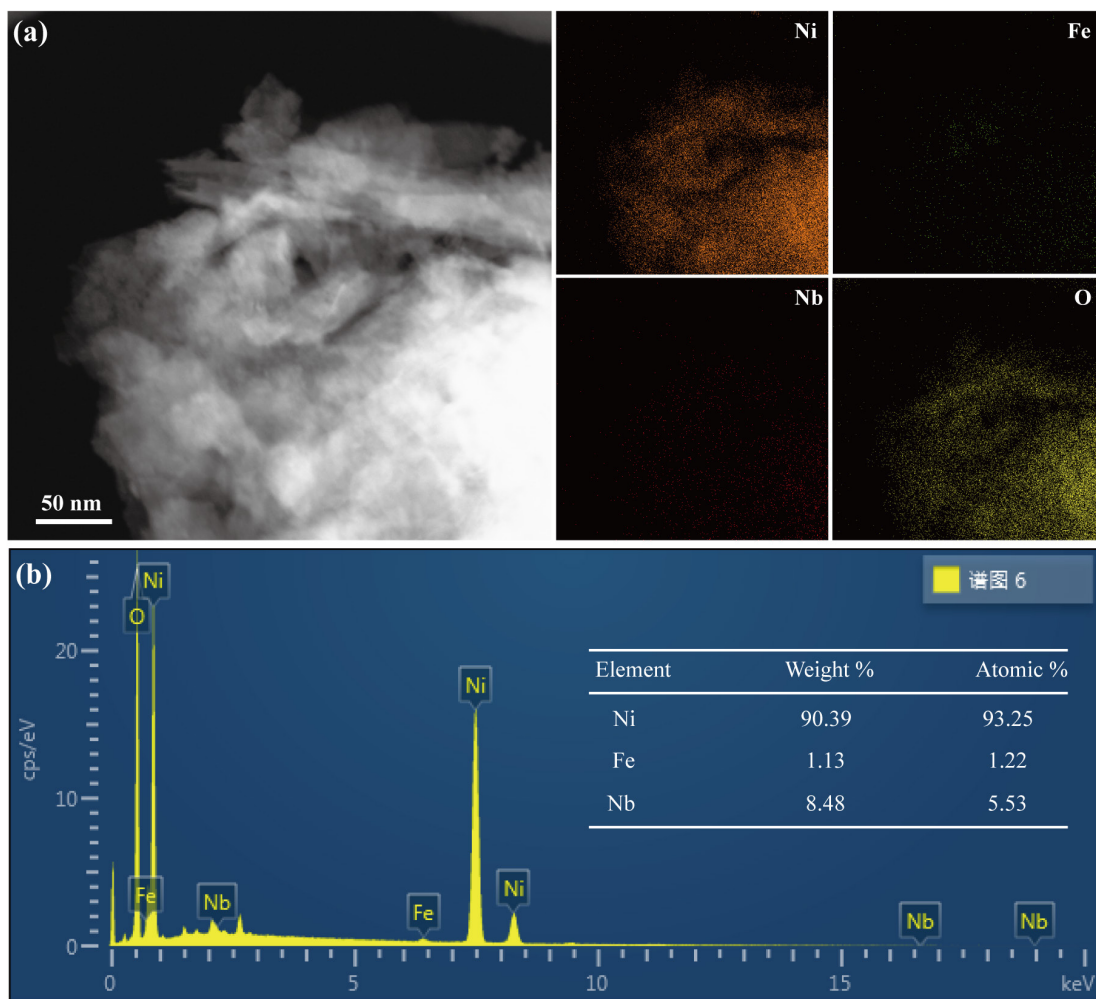**Fig. S5.** (a) TEM image and (b) HRTEM image of NiNb-OH (inset: the corresponding FFT transfer).

Fig. S6. (a) STEM image and corresponding elemental mappings of the NiFe$_1$Nb$_4$-OH, (b) EDS spectra of the NiFe$_1$Nb$_4$-OH.
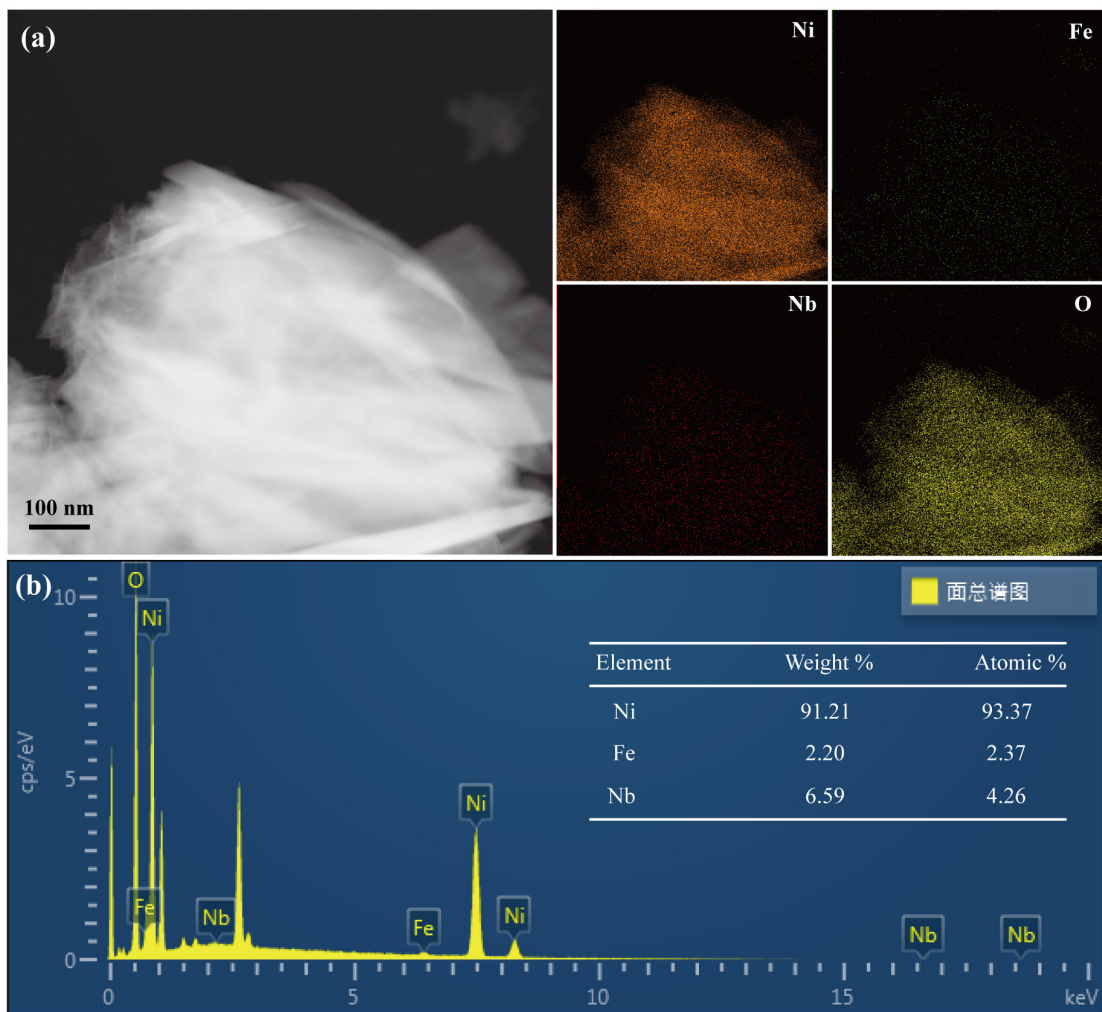
Fig. S7. (a) STEM image and corresponding elemental mappings of the NiFe$_2$Nb$_3$-OH, (b) EDS spectra of the NiFe$_2$Nb$_3$-OH.
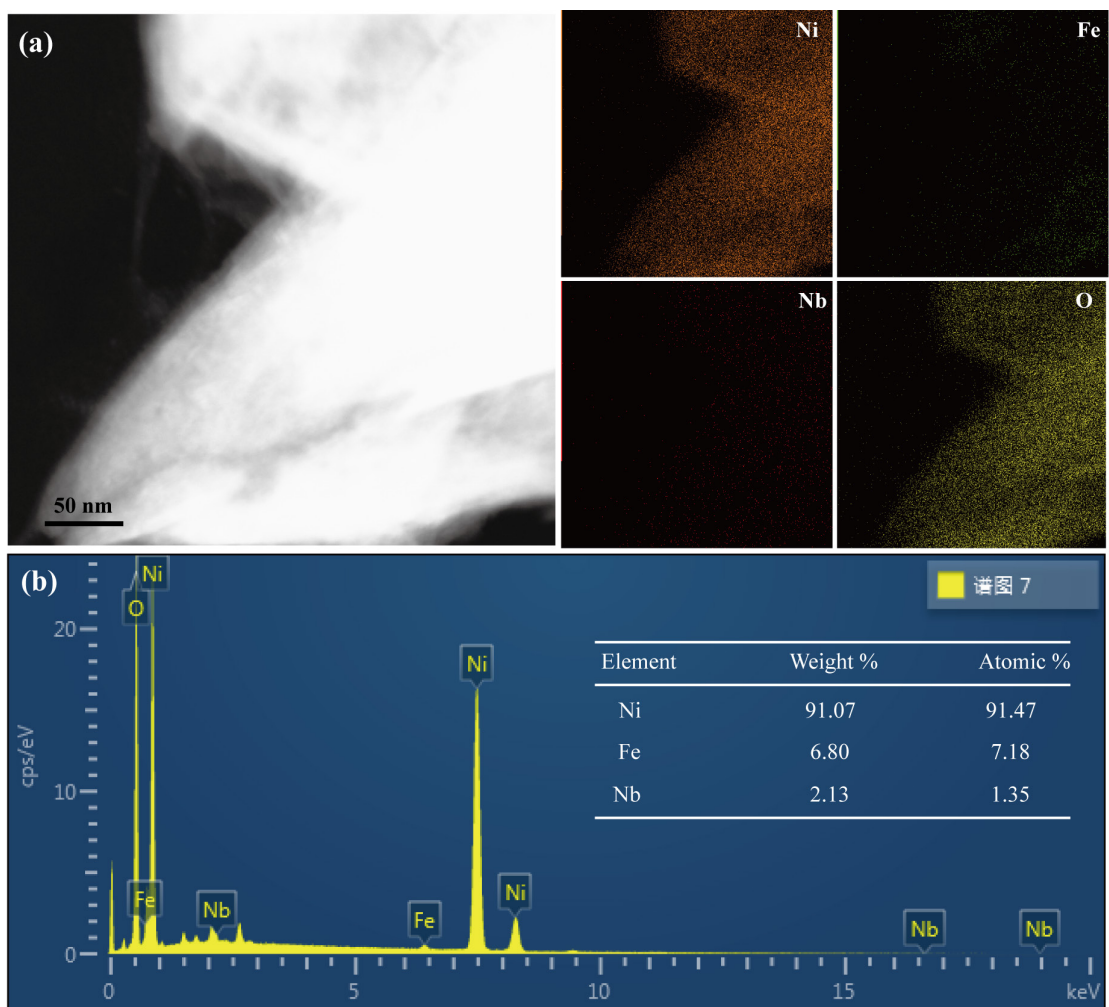
Fig. S8. (a) STEM image and corresponding elemental mappings of the NiFe$_4$Nb$_1$-OH, (b) EDS spectra of the NiFe$_4$Nb$_1$-OH.

Element	Weight %	Atomic %
Ni	91.07	91.47
Fe	6.80	7.18
Nb	2.13	1.35
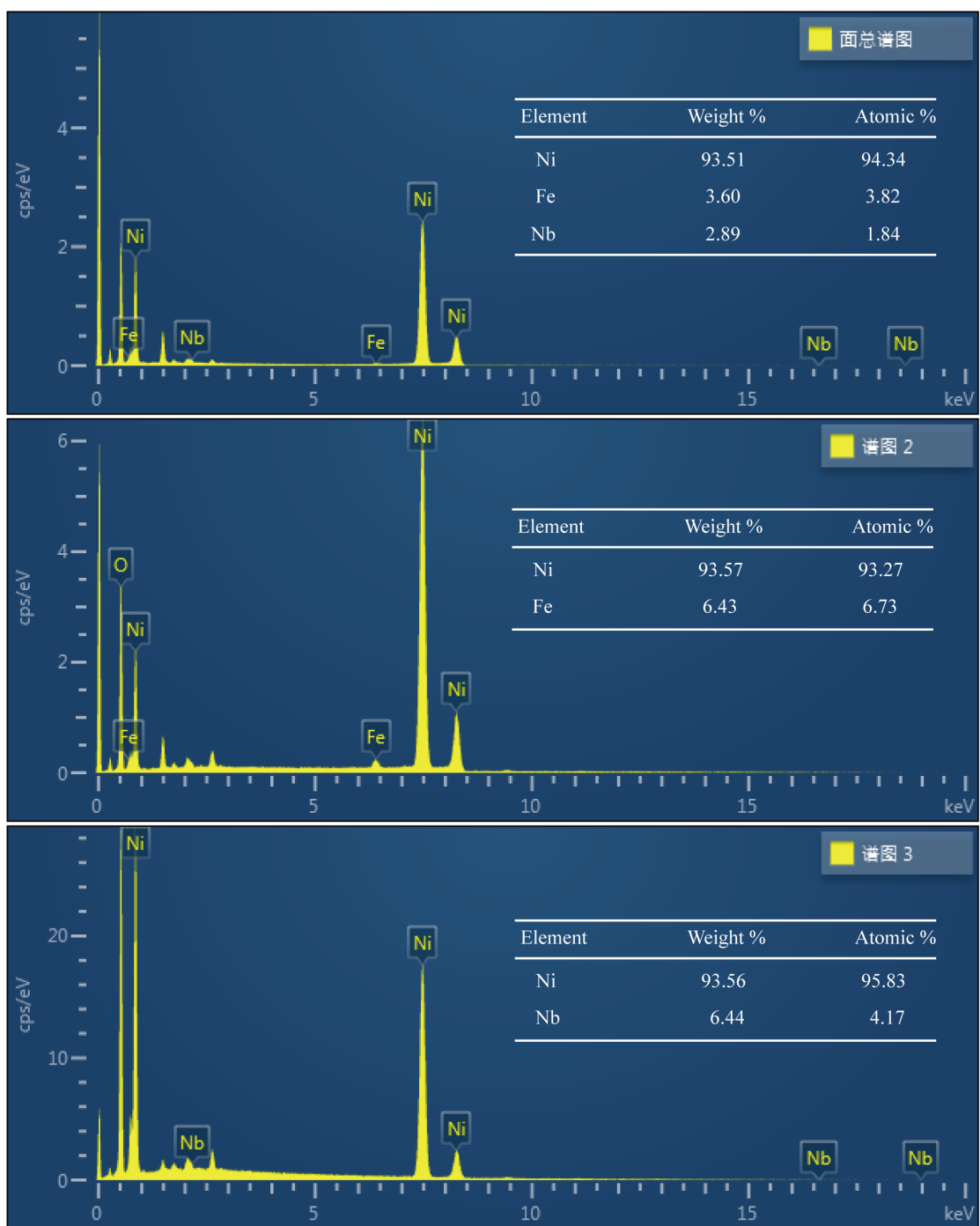
Fig. S9. EDS spectra for (a) NiFe$_3$Nb$_2$-OH, (b) NiFe-OH and (c) NiNb-OH.
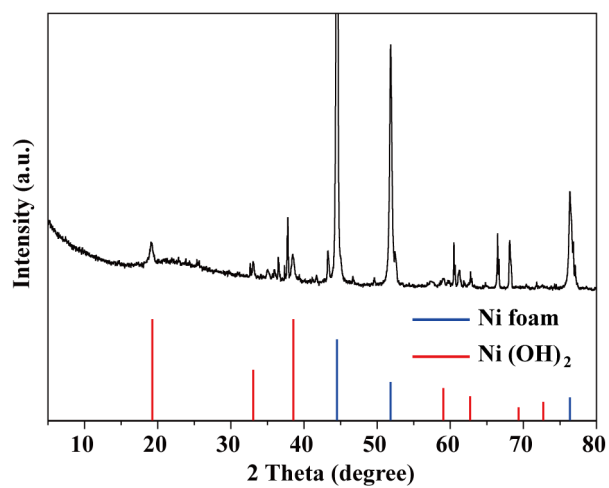
Fig. S10. XRD pattern of NiFe$_3$Nb$_2$-OH powders.
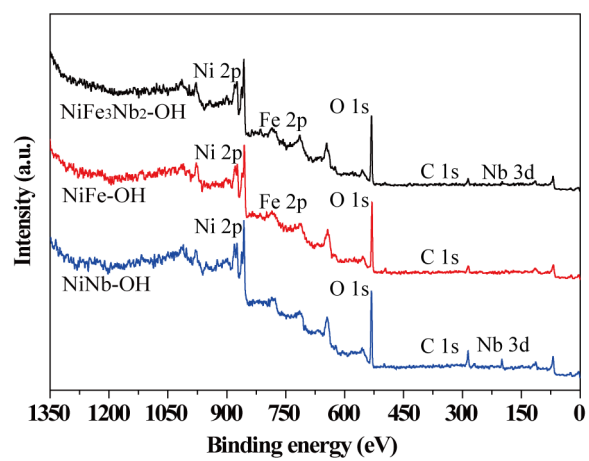
Fig. S11. XPS survey spectra of NiFe₃Nb₂-OH, NiFe-OH and NiNb-OH;
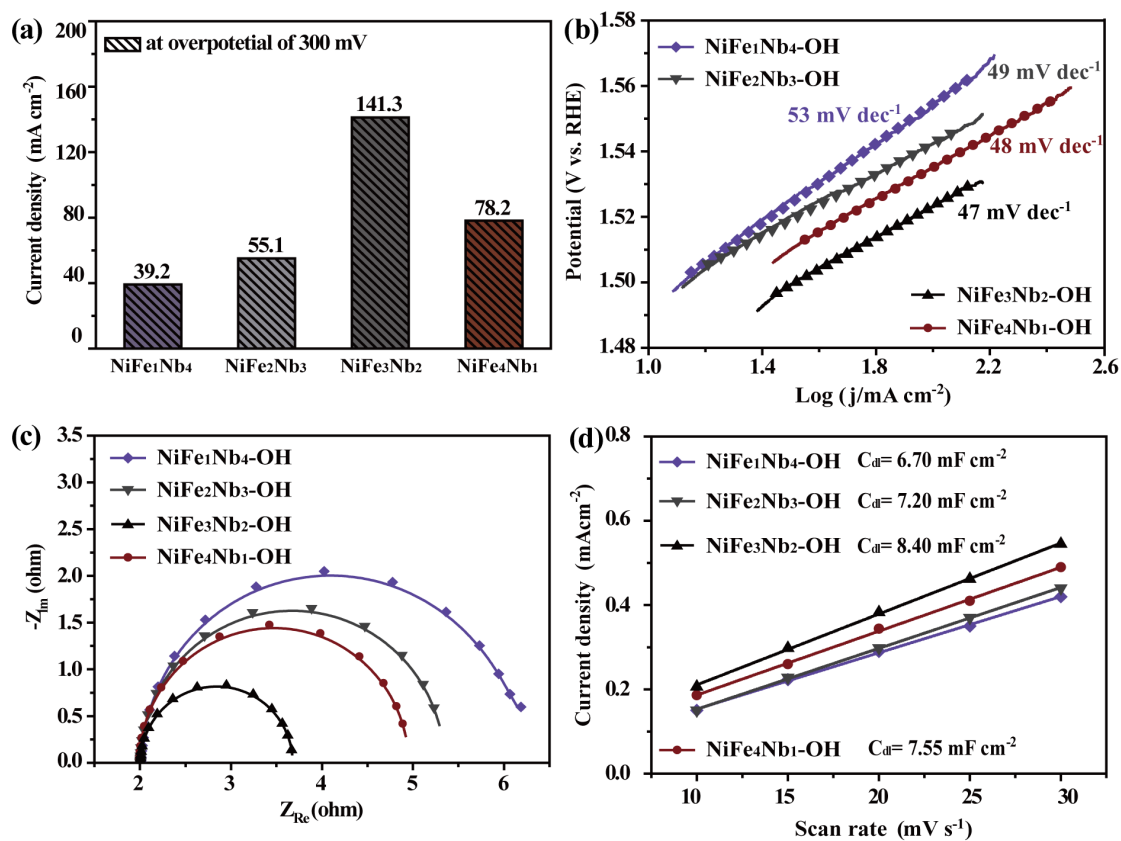
Fig. S12. (a) Current densities at overpotential of 300 mV, (b) Tafel plots, (c) Nyquist plots and (d) double-layer capacitances of NiFe$_1$Nb$_4$-OH, NiFe$_2$Nb$_3$-OH NiFe$_3$Nb$_2$-OH, and NiFe$_4$Nb$_1$-OH.
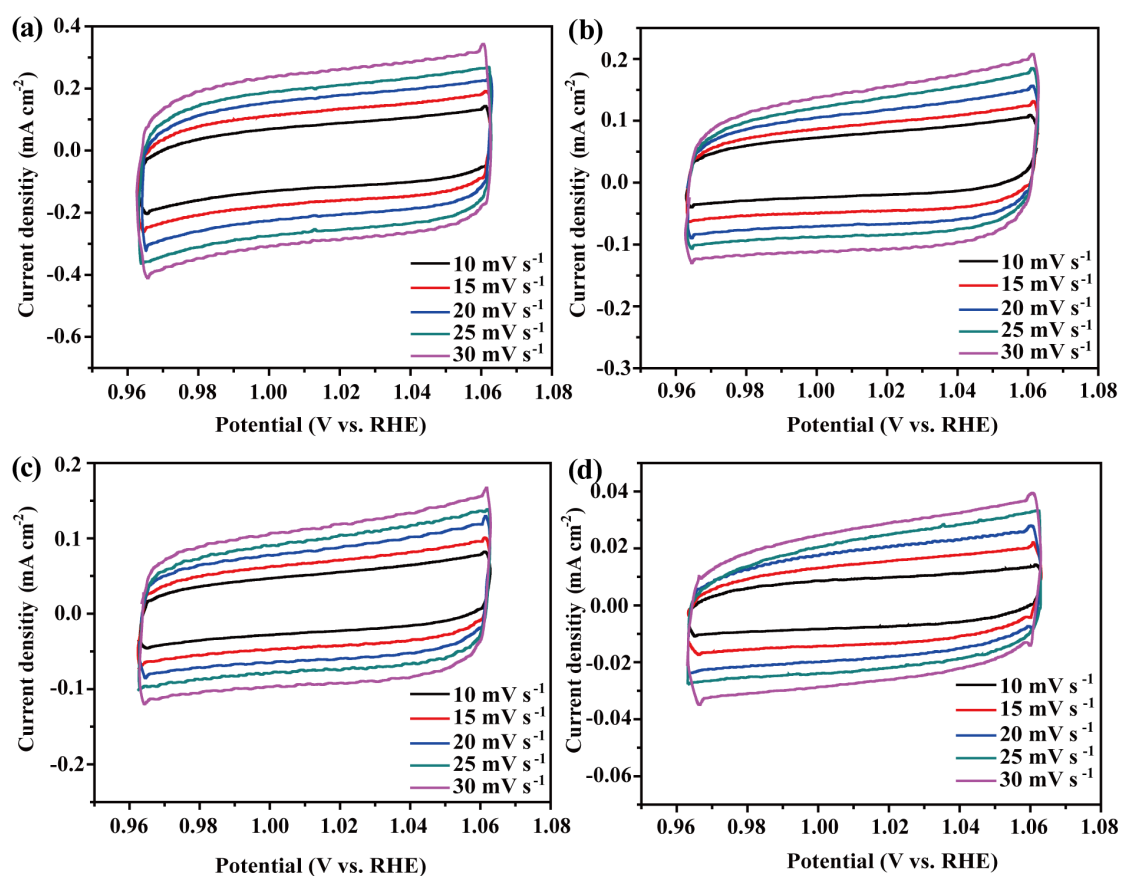
Fig. S13. Cyclic voltammograms of (a) NiFe$_3$Nb$_2$-OH, (b) NiFe-OH, (c) NiNb-OH and (d) blank Ni foam at various scan rates in the non-Faradic potential region.
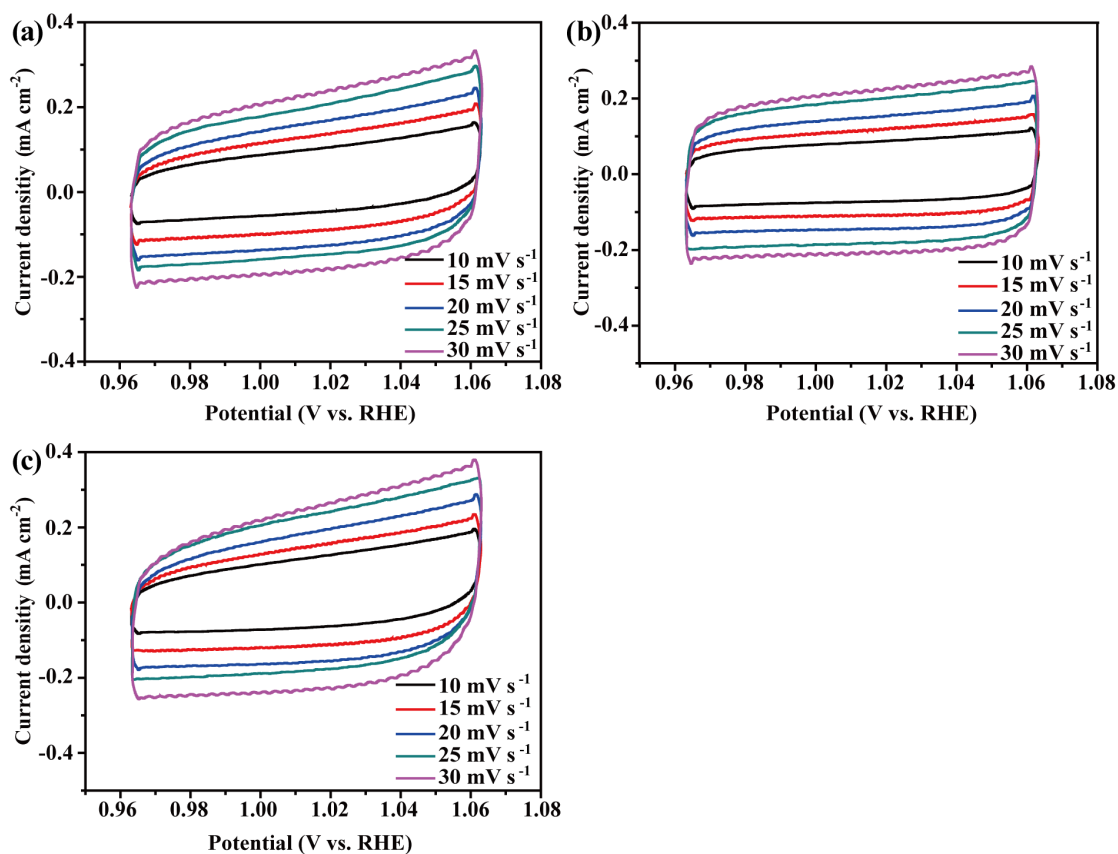
Fig. S14. Cyclic voltammograms of (a) NiFe$_1$Nb$_4$-OH, (b) NiFe$_2$Nb$_3$-OH and (c) NiFe$_4$Nb$_1$-OH at various scan rates in the non-Faradic potential region.
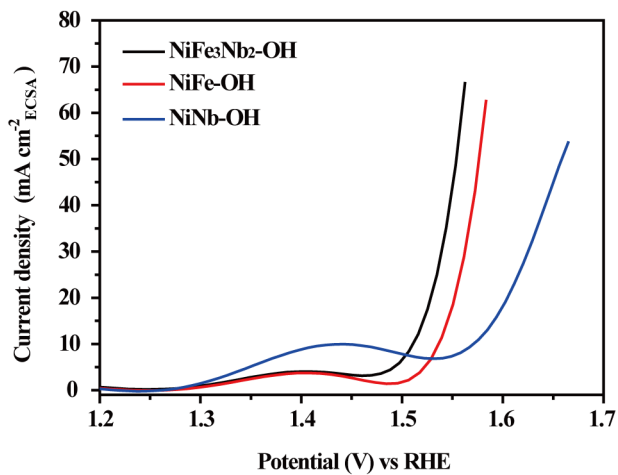
Fig. S15. ECSA normalized polarization curves of NiFe$_3$Nb$_2$-OH, NiFe-OH and NiNb-OH.
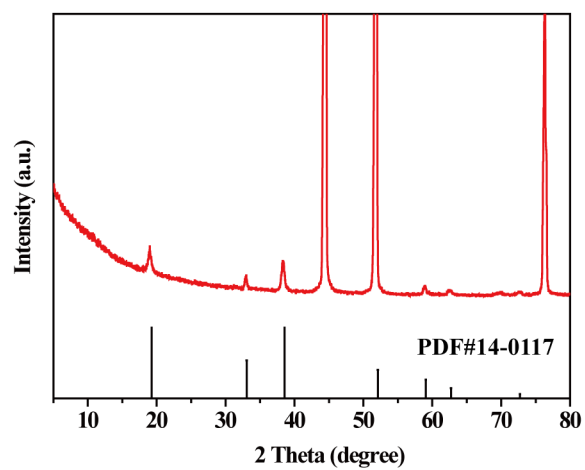
Fig. S16. XRD pattern of NiFe$_3$Nb$_2$-OH after stability test.
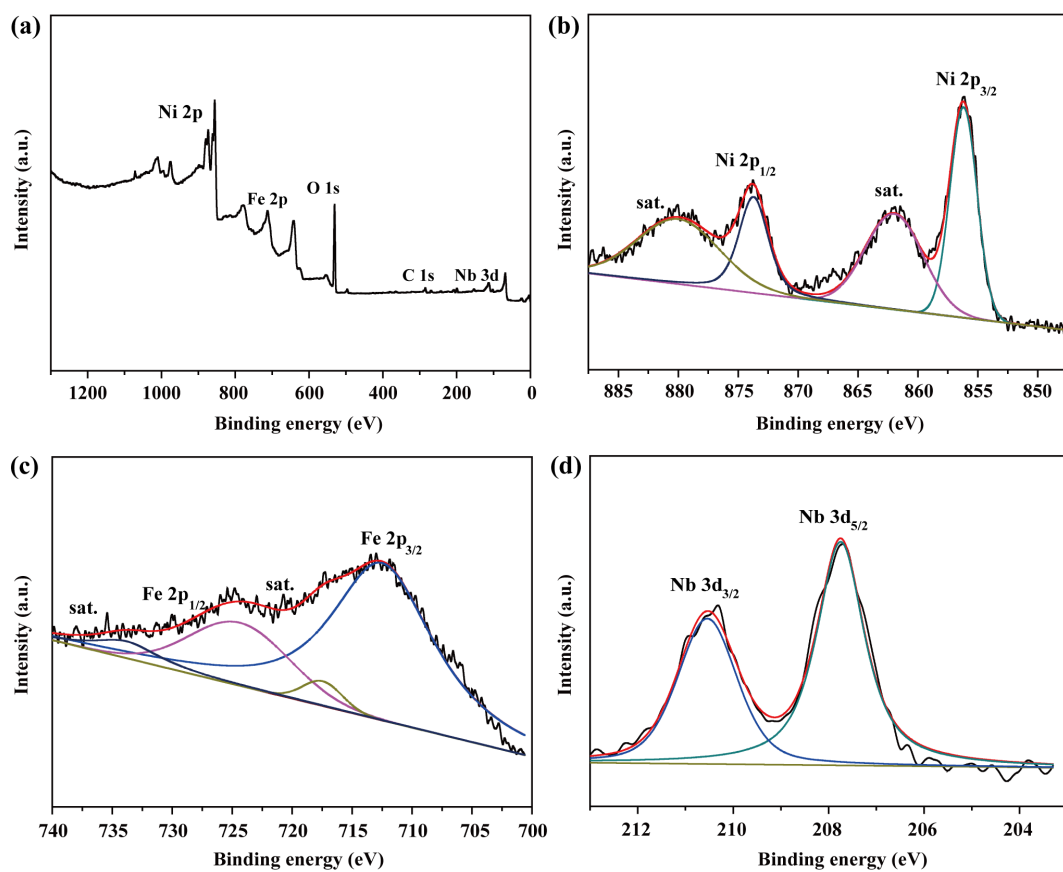
Fig. S17. XPS spectra of NiFe$_3$Nb$_2$-OH electrode after stability test: (a) survey spectrum, (b) Ni 2p, (c) Fe 2p, (d) Nb 3d.

Fig. S18. LSV curves of NiFeNb-OH, NiFe-OH and pure Ni(OH)$_2$.

Table S1. TOFs of NiFe$_3$Nb$_2$-OH and NiFe-OH at the overpotential of 300 mV.

	TOFs (s^{-1})		
Active site	Fe	Fe, Ni	Fe, Ni, Nb
NiFe$_3$Nb$_2$-OH	0.423	0.0164	0.0161
NiFe-OH	0.0437	0.0029	/

Table. S2. Comparison of OER activities of $NiFe_3Nb_2$-OH to other Ni based cataysts.

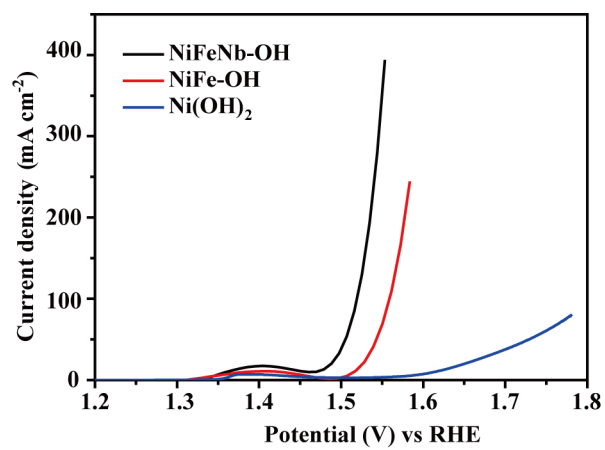| Catalysts	Electrolyte	Overpotemtial (mV)	Tafel slope (mV dec^{-1})	Catalysts
$NiFe_3Nb_2$-OH	1 M KOH	294 (100 mA cm^{-2})	47	This work
S-Ni(OH)$_2$	1 M KOH	338 (100 mA cm^{-2})	50	[2]
Ni@Co-Ni-P	1 M KOH	350(90.2 mA cm^{-2})	60	[3]
Ni–Co–S/CF	1 M KOH	363(100 mA cm^{-2})	109	[4]
Zn-Ni$_3$S$_2$/NF	1 M KOH	330(100 mA cm^{-2})	74	[5]
Ni-CoS$_2$/CC	1 M KOH	370(100 mA cm^{-2})	119	[6]
NWAs/NF	1 M KOH	370(100 mA cm^{-2})	54	[7]
Co$_{0.13}$Ni$_{0.87}$Se$_2$/Ti	1 M KOH	320(100 mA cm^{-2})	94	[8]
Ni$_{12}$P$_5$/Ni$_3$(PO4)$_2$	1 M KOH	318(100 mA cm^{-2})	51.7	[9]
FeNiOH/NF	1 M KOH	318(100 mA cm^{-2})	72	[10]
PE-NiMoP$_2$	1 M KOH	330(100 mA cm^{-2})	59.3	[11]
NiCo$_2$S$_4$ NA/CC	1 M KOH	340(100 mA cm^{-2})	89	[12]
NCP/G NSs	1 M KOH	400(100 mA cm^{-2})	65.9	[13]
NiMoO-SP/Ti	1 M KOH	360(100 mA cm^{-2})	85	[14]

Reference

1. J. K. Nørskov, J. Rossmeisl, A. Logadottir, L. Lindqvist, J. R. Kitchin, T. Bligaard and H. Jónsson, Origin of the Overpotential for Oxygen Reduction at a Fuel-Cell Cathode, *J. Phys. Chem. B*, 2004, **108**, 17886-17892.

2. M. Gao, L. He, Z.-Y. Guo, Y.-R. Yuan and W.-W. Li, Sulfate-Functionalized Nickel Hydroxide Nanobelts for Sustained Oxygen Evolution, *ACS Appl. Mater. Interfaces*, 2020, **12**, 443-450.

3. W. Li, X. Gao, X. Wang, D. Xiong, P.-P. Huang, W.-G. Song, X. Bao and L. Liu, From water reduction to oxidation: Janus Co-Ni-P nanowires as high-efficiency and ultrastable electrocatalysts for over 3000 h water splitting, *J. Power Sources*, 2016, **330**, 156-166.

4. T. Liu, X. Sun, A. M. Asiri and Y. He, One-step electrodeposition of Ni–Co–S nanosheets film as a bifunctional electrocatalyst for efficient water splitting, *Int. J. Hydrogen Energy*, 2016, **41**, 7264-7269.

5. Q. Liu, L. Xie, Z. Liu, G. Du, A. M. Asiri and X. Sun, A Zn-doped Ni3S2 nanosheet array as a high-performance electrochemical water oxidation catalyst in alkaline solution, *Chem. Commun.*, 2017, **53**, 12446-12449.

6. W. Fang, D. Liu, Q. Lu, X. Sun and A. M. Asiri, Nickel promoted cobalt disulfide nanowire array supported on carbon cloth: An efficient and stable bifunctional electrocatalyst for full water splitting, *Electrochem. Commun.*, 2016, **63**, 60-64.

7. J. Li, G. Wei, Y. Zhu, Y. Xi, X. Pan, Y. Ji, I. V. Zatovsky and W. Han, Hierarchical NiCoP nanocone arrays supported on Ni foam as an efficient and stable bifunctional electrocatalyst for overall water splitting, *J. Mater. Chem. A*, 2017, **5**, 14828-14837.

8. T. Liu, A. M. Asiri and X. Sun, Electrodeposited Co-doped NiSe2 nanoparticles film: a good electrocatalyst for efficient water splitting, *Nanoscale*, 2016, **8**, 3911-3915.

9. J. Chang, Q. Lv, G. Li, J. Ge, C. Liu and W. Xing, Core-shell structured $Ni_{12}P_5/Ni_3(PO_4)_2$ hollow spheres as difunctional and efficient electrocatalysts for overall water electrolysis, *Appl. Catal., B*, 2017, **204**, 486-496.

10. J.-T. Ren, G.-G. Yuan, C.-C. Weng, L. Chen and Z.-Y. Yuan, Uniquely integrated Fe-doped Ni(OH)2 nanosheets for highly efficient oxygen and hydrogen evolution reactions, *Nanoscale*, 2018, **10**, 10620-10628.

11. X.-D. Wang, H.-Y. Chen, Y.-F. Xu, J.-F. Liao, B.-X. Chen, H.-S. Rao, D.-B. Kuang and C.-Y. Su, Self-supported NiMoP2 nanowires on carbon cloth as an efficient and durable electrocatalyst for overall water splitting, *J. Mater. Chem. A*, 2017, **5**, 7191-7199.

12. D. Liu, Q. Lu, Y. Luo, X. Sun and A. M. Asiri, NiCo2S4 nanowires array as an efficient bifunctional electrocatalyst for full water splitting with superior activity, *Nanoscale*, 2015, **7**, 15122-15126.

13. J. Tian, J. Chen, J. Liu, Q. Tian and P. Chen, Graphene quantum dot engineered nickel-cobalt phosphide as highly efficient bifunctional catalyst for overall water splitting, *Nano Energy*, 2018, **48**, 284-291.

14. Y. Wang, T. Williams, T. Gengenbach, B. Kong, D. Zhao, H. Wang and C.

Selomulya, Unique hybrid Ni$_2$P/MoO$_2$@MoS$_2$ nanomaterials as bifunctional non-noble-metal electro-catalysts for water splitting, *Nanoscale*, 2017, **9**, 17349-17356.